Article

Charge Distribution and Bond Valence Sum Analysis of Sulfosalts—The ECoN21 Computer Program

Gheorghe Ilinca

Department of Mineralogy, University of Bucharest, Bd. N. Balcescu, 1, 010041 Bucharest, Romania; gheorghe.ilinca@g.unibuc.ro or g.g.ilinca@gmail.com

Abstract: The charge distribution (CD) and the bond valence sum (BVS) methods are used to calculate the charges assignable to atomic positions in crystal structures, based on the distribution of bond lengths. Discrepancies between calculated and formal charges may point to errors in the determination of atomic coordinates, in the initial allocation of oxidation numbers, occupancies, or site populations. Unlike the BVS method, which has been frequently used for the validation and interpretation of sulfosalt crystal structures, the CD method has been scarcely and limitedly employed for this group of minerals. In this paper, the applicability of the CD method to sulfosalts is practically tested for the first time. The calculation is made using ECoN21—a novel software tool designed for CD, BVS, and general coordination geometry analysis of crystal structures. The program addresses normal valence compounds with distorted homoligand or heteroligand polyhedra in both cation- and anion-centered descriptions. The program is also able to calculate a comprehensive set of parameters describing the internal and external distortion of coordination polyhedra. The paper presents the background of the CD, BVS, and coordination geometry calculations, as well as several case studies focusing on various applications of these methods to sulfosalts.

Keywords: charge distribution; bond valence sum; crystal structure; sulfosalts; polyhedral distortion; computer program

1. Introduction

In recent years, there has been a growing interest in deploying external measures for the evaluation and interpretation of various aspects of crystal structure refinement. For example, the bond valence sum (BVS) method (Brown [1–3]) has been applied to several sulfosalt structures, e.g., for refining the occupancies of mixed sites (e.g., Orlandi et al. [4], Biagioni et al. [5–7], etc.). This came as a normal consequence of the extreme isomorphic mobility of sulfosalts which often contain a significant number of mixed positions with uncertain proportions of endmembers. Due to the relatively easy calculation implied by the BVS approach, this has been the preferred, if not the exclusive, method used for this purpose. Nonetheless, the quality of the BVS analysis has always relied on the quality of the empirical parameters entailed by this method (e.g., R_o and B), which have been under continuous reevaluation and correction. For example, Biagioni et al. [7] invoked a wrongly refined R_o parameter extracted from the list published by Brese and O'Keefe [8], which resulted in several overbonded thallium positions in the crystal structure of Pb–rich chabournéite and for which the authors suggested an empirical correction.

Since the works of Hoppe [9] and Hoppe et al. [10], there has been little awareness of a self-reliant technique for attaining similar goals, namely, the charge distribution (CD) method. Notwithstanding the comprehensive works of Nespolo and his collaborators (Nespolo et al. [11,12], Eon and Nespolo [13], Nespolo and Guillot [14], Nespolo [15]), the CD method has gained little popularity as a means of assessing the quality of crystal structure determinations, especially for sulfosalts. The reason might reside in the complexity of the method—often not workable by manual or spreadsheet computation—and in the lack of

a software instrument able to handle the difficult calculations implied by the large and complicated crystal structures of this group of minerals.

While there are relatively numerous computer programs able to perform BVS calculations, only two are known to deal with the CD method. CHARDI2015 (Nespolo and Guillot [14]) is the most advanced and extensively documented application ever written for this purpose. Due to what appears to be a limitation of the maximum number of atoms accepted by the program, CHARDI2015 cannot run CD calculations for several large sulfosalt structures such as Pb-rich chabournéite (Biagioni et al. [7]), argentoliveingite (Topa et al. [16]), incomsartorite (Topa et al. [17]), dalnegroite (Bindi et al. [18]), and others. Another program able to perform CD computation is VESTA 3 (Momma and Izumi [19]). However, this program does not provide a batch-like solution for determining the CD across the entire set of coordination polyhedra in the structure. Besides, VESTA 3 does not calculate CD in heteroligand polyhedra.

A new computer program, ECoN21, was written in an attempt to extend the applicability of CD and BVS analysis to large sulfosalt crystal structures. Nevertheless, due to the underlying theoretical principles of the calculation, the program is also suitable for other types of inorganic normal valence compounds, including crystal structures with hydrogen bonds. The program can work with crystal structure data obtained from regular, in situ, or ab initio determinations. Since both methods convert bond lengths into bond strengths, they can be useful aids in the comparative and quantitative analysis of phase transitions at various temperatures and pressures.

The program addresses large homoligand and heteroligand crystal structures with distorted coordination polyhedra and significant isomorphic substitution. The main intention behind CD and BVS analysis is to signal wrong fractional coordinates expressed by wrong distances between the central atoms and their ligands, as well as erroneously assigned oxidation numbers and site populations in heterovalent mixed sites, especially when the atom content of such sites is characterized by similar scattering properties and cannot be properly refined in terms of endmember participation.

The paper aims to describe the CD method in the simplest way possible and to make it accessible to a wide range of users. All the structure representations in this paper were drafted with VESTA 3 (Momma and Izumi [19]).

2. The Calculation Procedure

2.1. The Charge Distribution Method

The second rule of coordination (Pauling [20]) states that in a stable crystal structure, the charge q_A of each anion in a coordination polyhedron (CP) tends to compensate for the *strength of the electrostatic valence bonds* reaching it from the central cation carrying a charge q_X:

$$q_A = -\sum_i \left(\frac{q_X}{CN}\right)_i = -\sum_i s_i, \tag{1}$$

where CN is the coordination number and s_i is the (Pauling's) bond strength. This equation applies only to regular polyhedra (e.g., Figure 1a). Instead, irregular polyhedra (e.g., Figure 1b) require a bond length–bond strength relationship to describe the decrease of the bond strength with increasing bond length.

Both the CD and BVS methods involve power laws that express this relationship. The differences between the two methods have been extensively described (e.g., Nespolo et al. [11]). In the case of the CD method, the bonds of a CP are ranked according to their length. Each bond is assigned a bond weight that will determine the relative strength of that bond. The shortest distance will receive the maximum bond weight and all the other weights will be scaled down following a negative exponential law. This is possible only if all the ligands in a CP are of the same chemical variety. If more chemical species of ligands coexist in a CP, then each chemical type of ligand must have its minimum distance as the scaling parameter. In the most general case, a CP will consist of a central atom surrounded by ligands of different chemical types, situated at different distances, that is,

of a distorted heteroligand CP. To establish the shortest bond length for each chemical type, the heteroligand polyhedron is divided into several homoligand subpolyhedra (HSP) (Nespolo [15]) (Figure 1c).
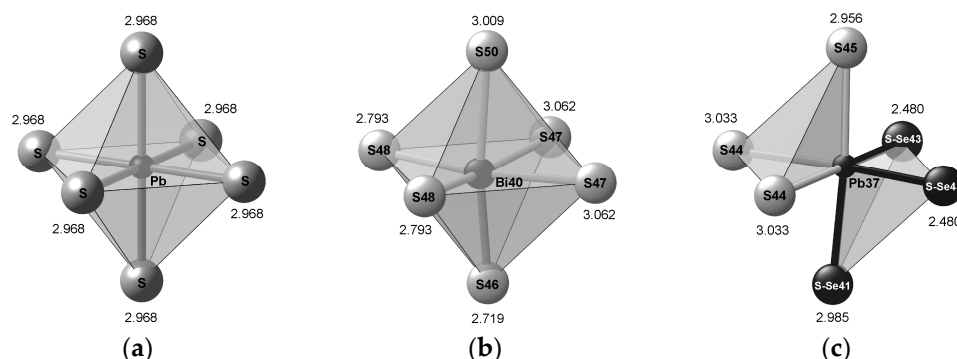

Figure 1. Examples of coordination polyhedra: (**a**) regular coordination octahedron in galena (AM-CSD 0011372 and reference therein); (**b**) irregular homoligand octahedron around the Bi40 position in cannizzarite (Topa et al. [21]); (**c**) irregular heteroligand octahedron around the Pb37 in the same crystal structure, with two homoligand subpolyhedra defined for pure S and mixed S-Se ligands. The values near the octahedra's vertices are bond lengths in ångstroms.

An HSP may contain only one ligand that is implicitly assigned the maximum bond weight, but which may result in an overestimated bond strength at the CP scale. For this reason, the CD calculation for heteroligand CP must include an iteration procedure which is described later in this section.

The notation used in this section largely follows the symbolism used by Ferraris [22]. In general, the terms 'cation' and 'anion' have been avoided throughout the presentation of the calculation procedures. References are made only to the terms 'central atom' and 'ligand'. Thus, the formulas can be used reversely for the cation-centered or anion-centered descriptions of the structure, with just the appropriate change of sign and symbol.

The enumeration indexes used in the calculation are the following:

- i—the index of ligands in an HSP;
- j—the index of HSPs in a CP;
- X—the index of crystallographic species of central atoms (or of distinct CP);
- A—the index of crystallographic species of ligands.

For a given CP, a self-consistent bond length–bond strength relationship is established through the calculation of the *bond weights* w_{ij} for each ligand in HSP_j (Hoppe et al. [10]):

$$w_{ij} = \exp\left[1 - \left(\frac{R_{ij}}{\overline{R}_j}\right)^6\right], \tag{2}$$

where $\overline{R}_j$ is the weighted average bond distance calculated through an iteration process converging after N steps:

$$^N\overline{R}_j = \frac{\sum_i R_{ij}\, exp\left[1 - \left(\frac{R_{ij}}{^{N-1}\overline{R}_j}\right)^6\right]}{\sum_i exp\left[1 - \left(\frac{R_{ij}}{^{N-1}\overline{R}_j}\right)^6\right]} \tag{3}$$

The starting term $^0\overline{R}_j$ ($N = 1$) represents the shortest (i.e., the 'strongest') bond in the jth HSP. The iteration procedure was devised by Nespolo et al. [12] to improve the approximation of $^N\overline{R}_j$ in highly deformed polyhedra.

The exponent 6 in the equations above is an empirical constant introduced by Hoppe [9] to approximate the decrease rate of bond weights with increasing bond lengths. Whenever explicit hydrogen bonds are present in the crystal structure (i.e., hydrogen atoms with listed fractional coordinates and +1 charge), the exponent 6 in Equations (2) and (3) changes to 1.6. This particular value was refined by Nespolo et al. [12] using a large number of structures, and it was meant to prevent the rapid fall of hydrogen bond weights with increasing bond distances.

The *effective coordination number* ($ECoN_X$) is calculated for each CP as the sum of all bond weights:

$$ECoN_X = \sum_j \sum_i w_{ij} \tag{4}$$

$ECoN_X$ is a real number, smaller than or equal to CN. $ECoN_X$ becomes identical to CN only in the case of regular polyhedra, where all R_{ij} and w_{ij} values are identical.

The charge of a central atom X, i.e., the formal oxidation number q_X, is distributed to all the ligands in proportion to the fractional bond weight $w_{ij}/ECoN_X$. The *partial charge* $\Delta q_{Xij \to A}$ (corresponding to Pauling's bond strength) received by a ligand A from the central atom X, is given by:

$$\Delta q_{Xij \to A} = q_X \frac{w_{ij}}{ECoN_X} \frac{m_X}{m_A} \tag{5}$$

The ratio of multiplicities m_X/m_A ensures that ligands of a certain crystallographic type are counted in the necessary amount and that they receive the right fraction of charge. The *total charge* Q_A of the Ath ligand is obtained through summation of partial charges received by A in every CP it belongs to:

$$Q_A = -\sum_X \Delta q_{Xij \to A} \tag{6}$$

and should be as close as possible to the formal charge of the Ath ligand, namely, q_A.

The *total charge* Q_X received back by the Xth central atom from its ligands is:

$$Q_X = \sum_j \sum_i \Delta Q_{ij} = \sum_j \sum_i \Delta q_{Xij \to A} \frac{q_A}{Q_A} \frac{m_A}{m_X} \tag{7}$$

Thus, any q_A/Q_A imbalances occurring in the coordination environment of the central atom will influence the value of Q_X which should be as close as possible to the formal oxidation number q_X.

In the case of homoligand structures, the calculation stops here. For heteroligand structures, further steps are taken by correcting the partial computed charges ΔQ_{ij} received by the central atom X, with the q_X/Q_X ratio and by summing the new values for each HSP_j:

$$\Delta Q_j = \sum_i \Delta Q_{ij} \frac{q_X}{Q_X} \frac{m_X}{m_A} \tag{8}$$

Also, for each HSP_j, the partial charges are summed up:

$$\Delta q_j = \sum_i \Delta q_{Xij \to A} \tag{9}$$

The ratio $\Delta Q_j / \Delta q_j$ is then used to do the calculation once more, with a new set of $\Delta q_{Xij \to A}$:

$$^N\Delta q_{Xij \to A} = \frac{\Delta Q_j}{\Delta q_j} {}^{N-1}\Delta q_{Xij \to A} \tag{10}$$

Alternatively, ΔQ_j can be summed up from the $\Delta Q_{ij \leftarrow X}$ calculated for the ligands of the X atom when observed in their ligand-centered environment. Thus, ΔQ_j will correspond to the $\Delta Q(ij \to r) = -\Delta Q(i \to rs)$ swap in the iteration procedure described by Nespolo [15]

and used by the program CHARDI2015. Both iteration methods are included in the ECoN21 program. The calculation can be repeated until convergence is reached for a given threshold T, e.g., expressed as the maximum difference between successive ΔQ_j:

$$^N\Delta Q_j - {}^{N-1}\Delta Q_j \leq T \tag{11}$$

The calculated charges for the central atom are collected from the last Q_X sums and the ligand charges from the last Q_A values. A graphic representation of the charge distribution is shown in Figure 2.
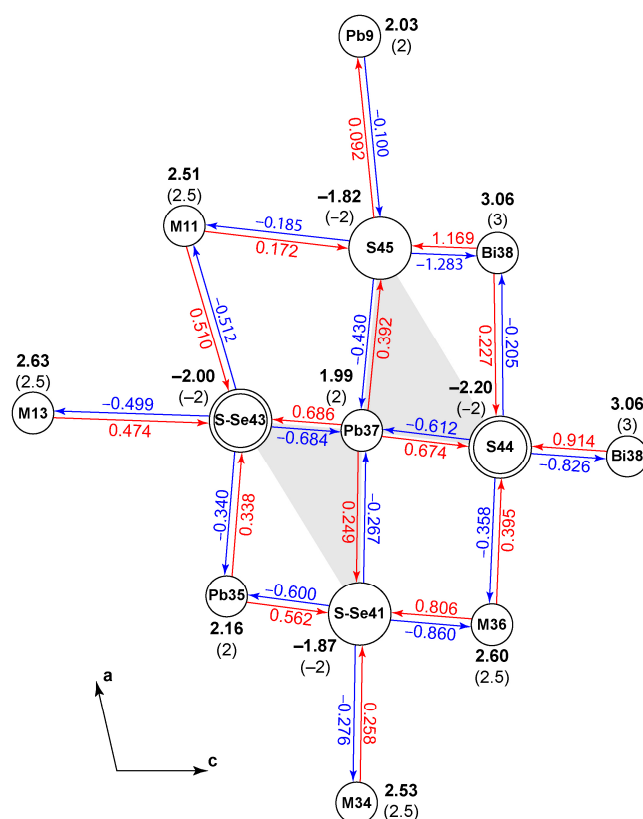

Figure 2. The charge distribution around Pb37 in the structure of cannizzarite (Topa et al. [21]). The formal charge of Pb37 ($q_X = 2$) is distributed to the ligands in proportion to the fractional weight of each bond (red arrows diverging from Pb37). The red figures are $\Delta q_{Xij \to A}$ values calculated with Equation (5). The total charge Q_A (e.g., -2.204 for S44) received by each ligand, is the sum of $\Delta q_{Xij \to A}$ from all the surrounding central atoms (red arrows converging to each ligand). The total charge $Q_X = 1.991$ received back by Pb37 from its ligands (blue arrows converging to Pb37) is the sum of ΔQ_{ij} values calculated with Equation (7) (blue figures). Ideally, Q_X and Q_A should match the formal oxidation numbers q_X and q_A, respectively (e.g., +2 for Pb37 and -2 for S44, S45, S–Se41, S–Se43). Figures in bold lettering are the computed charges—Q_X and Q_A—with the formal oxidation numbers—q_X and q_A—in parentheses. M11, M13, M34, M36 symbols stand for mixed 0.5Pb–0.5Bi positions ($q_X = 2.5$). Double outlined circles represent pairs of crystallographically similar sulfur atoms overlapping along the b axis. The shaded areas are projections of the two HSPs defined for the Pb37 CP.

The overall deviations of Q_X and Q_A from q_X and q_A are checked through the calculation of the *mean absolute percentage deviation* (*MAPD*) (Eon and Nespolo [13]). As an example—for the entire set of NX central atoms in the asymmetric unit—*MAPD* is calculated as:

$$MAPD_{Q_X}(\%) = \frac{100}{NX}\sum_X \left| \frac{q_X - Q_X}{q_X} \right| \tag{12}$$

2.2. The Bond Valence Sum Method

In the case of the BVS method, *partial valences* s_{ij} (analogs of Pauling's bond strength) are assigned to each bond of a CP, in correlation with their bond length. The correlation entails empirical exponential curves defined for specific cation-anion pairs and fitted from a large number of structures. Of several equalities describing this correlation, ECoN21 uses Equation (13) (Brown and Altermatt [23]):

$$s_{ij} = \exp\left(\frac{R_{oij} - R_{ij}}{B_{ij}}\right) \qquad (13)$$

This equation was chosen mainly for the abundance of accumulated empirical parameters R_{oij} and B_{ij} that have been established for nearly all possible cation-anion bonds (Brown [24]) and which are available to ECoN21 via a dedicated file. The term R_{oij} represents the nominal length for a bond of unit valence, while B_{ij} denotes the 'softness factor', which, in the early works of Brown and Altermatt [23] and subsequent collections of bond valence parameters (e.g., Brese and O'Keeffe [8]) was considered constant, equal to 0.37 Å. In recent years, B_{ij} for metal-oxygen bonds, has been subjected to ample refinements (e.g., Gagné and Hawthorne [25]) which established different values for this parameter. However, for pairs of ions commonly occurring in sulfosalts, B_{ij} values are still listed with the original constant. The term R_{ij} represents the *i*th bond length in HSP_j. Due to its dependence on empirical parameters, the treatment of s_{ij} in mixed positions may be prone to systematic errors (Bosi [26]). In this stage of development, the program approximates the s_{ij} assuming that mixed sites are occupied simultaneously by fractional endmembers. The *bond valence sum* for an entire CP with central site occupancy $SOF \leq 1$ is:

$$BVS_X = SOF \sum_j \sum_i s_{ij} \qquad (14)$$

Ideally, the BVS_X calculated for a given CP should match the oxidation number q_X of the central atom. Based on this formal charge and using Equation (13), the *expected bond distances* for each ligand in the CP can be calculated:

$$ER_{ij} = R_{oij} - ln\left(s_{ij}\frac{q_X}{BVS_X}\right)B_{ij} \qquad (15)$$

The correction factor q_X/BVS_X applies to all the bond lengths in a CP, and therefore it expands or condenses the entire CP to match q_X. The same type of equation as in (12) is used to obtain the $MAPD$ for the entire set of BVS_X.

The *global instability index* (Brown [27]) is used as a measure of the crystal structure strain: in well-balanced and stable structures, the index is smaller than 0.1 v.u.; strained structures yield an index between 0.1 and 0.2 v.u., whereas well–determined structures with the global instability index greater than 0.2 v.u. are considered to be rare. For the set of NZ atoms (cations and anions) in the formula unit, it is calculated as:

$$GII = \sqrt{\frac{1}{NZ}\sum_Z (BVS_Z - q_Z)} \qquad (16)$$

The *relative charge error* is obtained with:

$$EV(\%) = 100\left|\frac{TX - TA}{TX}\right|, \qquad (17)$$

where TX is the total charge of the cations and TA, the total charge of the anions, calculated from the structure-derived formula.

2.3. Coordination Geometry

The CD and BVS calculations are significant only in the context of distorted coordination polyhedra. For this reason, a part of the ECoN21 program is dedicated to the actual geometry of the CP. As shown by Makovicky and Balić–Žunić [28], two types of distortion may be considered: (1) an internal distortion given by the displacement of the central atom and by the irregularity of the bond lengths and angles and (2) an external ('volume') distortion determined by the departure of the ligands from the ideal surface of a least-squares fitted (LSF) or 'circumscribed' sphere which approximates their distribution. Both types may be analyzed using quantities related to the 'centroid' of the CP (Makovicky and Balić–Žunić [29], Balić–Žunić, and Vicković [30]), that is, to the point against which the variance of squared distances to the ligands is minimum:

$$\Delta RC = \sum_k \left(RC_k^2 - \frac{\sum_k RC_k^2}{CN_X} \right)^2 \tag{18}$$

where RC_k represents the kth centroid–ligand distance. The following values are calculated by ECoN21 using the definitions and the procedures published by Makovicky and Balić–Žunić [28,29] and included in the MS-DOS program IVTON (Balić–Žunić and Vicković [30]):

- *the coordinates x_o, y_o, z_o of the centroid*—obtained by expressing Equation (18) in terms of orthogonal coordinates and by solving the linear system formed by the partial derivatives for x_o, y_o, and z_o which are set equal to zero;
- *the components I, J, and K of the vector between the centroid and the central atom*—indicating the direction opposite to the lone electron pair of the central atom;
- *the displacement Δ of the central atom from the centroid;*
- *the radius r_s of the LSF sphere*—represented by the average distance between the centroid and the ligands;
- *the volume V_s of the LSF sphere;*

  The definitions of quantities in Equations (19)–(22) were explained in Topa et al. [31].
- *the linear eccentricity of the central atom:*

$$LEcc = \frac{\Delta}{r_s}; \tag{19}$$

- *the 'volume-based' eccentricity of the central atom,* obtained by comparing the volume of the LSF sphere with the volume of the sphere of radius $(r_s - \Delta)$:

$$VEcc = 1 - \left[\left(1 - \frac{\Delta}{r_s} \right) \right]^3; \tag{20}$$

- *the linear sphericity of the ligand distribution*:

$$LSph = 1 - \frac{\sigma_s}{r_s}, \tag{21}$$

  where σ_s is the standard deviation of the centroid–ligand distances;
- *the 'volume-based' sphericity of the ligand distribution*:

$$VSph = 1 - \frac{3\sigma_s}{r_s}; \tag{22}$$

- *the volume V_r of the CP* obtained by dividing the CP into tetrahedra delimited by triplets of adjacent vertices and the central atom, and by summation of their volumes;
- *the approximation of the ideal polyhedron of maximum volume inscribed in the LSF sphere*—established as a function of CN_X and number of CP faces;

- *the volume V_i of the ideal polyhedron inscribable in the LSF sphere and which has the maximum possible volume for that sphere;*
- *the volume distortion of the CP:*

$$v = 1 - \frac{V_r}{V_i};$$ (23)

In addition to the parameters derived from the centroid, the following indicators of polyhedral distortion are calculated:

- *the deviation of $ECoN_X$ from CNR_X :*

$$EDEV_X = 1 - \frac{ECoN_X}{CNR_X},$$ (24)

where CNR_X is the number of ligands with bond weights exceeding 0.001 (thus, $EDEV_X$ does not depend on a CN_X resulting from an arbitrary setting of the coordination radius);

- *the distortion index $\Delta R(Ba)$ of a CP* (Baur [32]):

$$\Delta R(Ba) = \frac{1}{CN_X} \sum_j \sum_i \frac{\left| R_{ij} - \overline{R}_X \right|}{\overline{R}_X},$$ (25)

where $\overline{R}_X$ is the average bond length to all the CN_X ligands in the CP;

- *the bond valence-based distortion index $\Delta R(Br)$* (Brown [27]):

$$\Delta R(Br) = -\frac{B}{CN_X} \sum_j \sum_i \ln\left(\frac{s_{ij}}{\overline{s}_X}\right),$$ (26)

where $\overline{s}_X$ is the average bond valence over all ligands. In this equation, $\Delta R(Br)$ is independent of the empirical parameter R_{oij}. As long as the B_{ij} parameter is constant ($= B$) for all R_{ij} bonds, $\Delta R(Br)$ can be used to calculate the polyhedral distortion also for heteroligand environments.

For each CP in the structure, the program calculates bond and dihedral angles and interligand distances, as well as distances to the surrounding central atoms within a 5Å threshold.

3. The ECoN21 Program

3.1. General Features

The name of the program derives from Effective Coordination Number which is a central concept in CD analysis. The term was coined by Rudolf Hoppe in 1979, with a view to a better characterization of distorted coordination polyhedra which are set apart by the anisotropic distribution of bond strengths.

ECoN21 is a standalone program requiring no installation or additional dynamic libraries. It was written in Delphi and developed in Embarcadero RAD Studio 10.4 CE, both as Windows 32 and 64-bit applications. The program was tested with 32 and 64-bit Windows 7 and later versions, and it is available for download at: https://unibuc.ro/user/gheorghe.ilinca/?profiletab=documents (accessed 15 July 2022) or by e-mail from gheorghe.ilinca@g.unibuc.ro or g.g.ilinca@gmail.com.

ECoN21 has a rather self-explanatory user interface (Figure 3). The user must open a CIF file, check whether the file was read correctly, run the calculation, and get the results, both on-screen and in an output file.

Before running the calculation, the user can adjust the coordination radius thresholds for searching ligands around a central atom. This can be achieved using either of the following methods: (1) a unique threshold applied to the entire crystal structure, (2) separate thresholds for each type of chemical bond, or (3) custom coordination radii for each CP. The automatic limitation of coordination thresholds based on non-zero bond weights and/or the

distance to the closest central atom is also possible. The latter option prevents neighboring central atoms from being included in the coordination sphere established through global or bond type-specific thresholds.
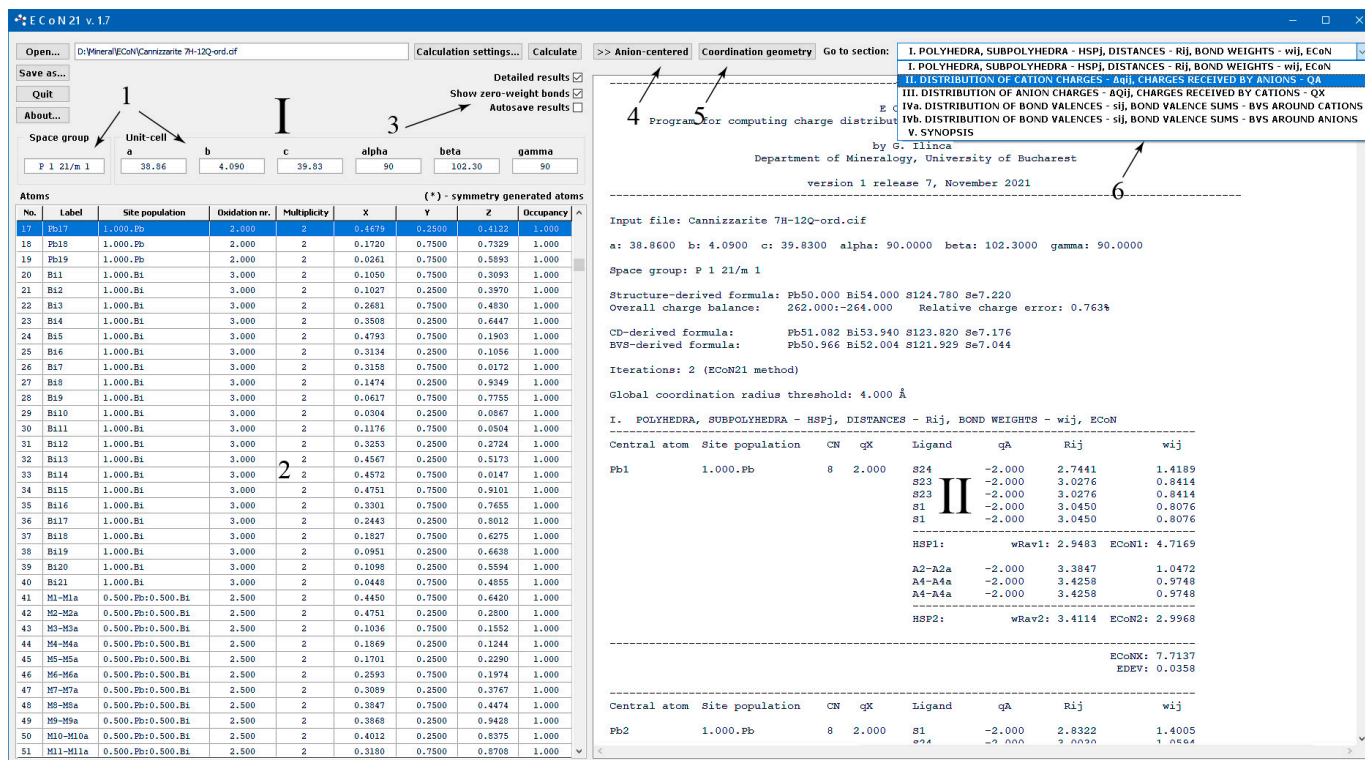

Figure 3. The interface of the ECoN21 program: (I) input panel; (II) results panel; (1) space group and unit–cell parameters panels; (2) atoms table; (3) visualization and save options; (4) switch to anion-centered view; (5) button for visualization of coordination geometry; (6) navigation aid for long outputs.

The program runs the BVS calculation automatically by collecting the R_{oij} and B_{ij} parameters from a dedicated file which is a slightly modified version of the *bvparm2020.CIF* file (Brown [24]) issued by IUCr. The file containing the R_{oij} and B_{ij} can be edited and updated.

The only type of input accepted by ECoN21 is a CIF file with the following mandatory content:

- unit cell parameters
- symmetry operators
- atom labels
- atom symbols
- oxidation numbers
- fractional coordinates
- occupancies

Several CIF formats have been tested so far, including ICSD, AMCSD, COD, and Jana2006 (Petříček et al. [33]). Depending on the source, it may sometimes be necessary to add the atom symbols, oxidation numbers, occupancies, etc., by hand. Details on how and where to add these values as well as on the necessary content and syntax of the CIF file are given in the comprehensive manual accompanying the program.

Fragments of the Delphi source code and a presentation of the code units used to build ECoN21 are included in Supplementary Materials S13.

3.2. Interpreting the Results

The estimation of the overall correctness of the crystal structure model and the interpretation of the oxidation numbers assigned to monoelemental or (heterovalent) mixed sites are made in very simple terms and should rely on the following criteria:

- the Q_X, Q_A, and BVS_X values should be close to their corresponding formal oxidation numbers q_X or q_A, respectively. Consequently, the departure from 1.0 of the q_X/Q_X and q_A/Q_A ratios may also be used to assess the matching between the formal and calculated charges. In the cation-centered description, the q_X/Q_X ratio gives a measure of the overall geometric correctness of the structure (atom coordinates, distances), whereas q_A/Q_A points to the over- or underbonding effects induced by inadequate calculated charges of the central atoms (e.g., Nespolo et al. [11,12]), making it suitable for measuring the effects of compositional changes in central heterovalent mixed positions. In the anion-centered description, the significance of the two ratios is reversed.

- the mean absolute percentage deviation $MAPD$ (Eon and Nespolo [13]) of Q_X, Q_A, or BVS_X from the nominal oxidation numbers (q_X or q_A) for the entire structure or selected clusters of atoms. These values should be as close as possible to 0%. It may be roughly estimated that global $MAPD$s calculated for the central atoms and larger than 10% point out negative issues in the refinement of the crystal structure. Elevated $MAPD$s for global or local ligands should draw attention to potentially misassigned oxidation numbers of the central atoms.

More advanced interpretations may result from the use of collateral parameters calculated by the program, such as $ECoN_X$ or $EDEV_X$, and by analyzing their relationship with various parameters describing the distortion of coordination polyhedra (see Section 2.3 and the case study Section 4.4 in this paper).

4. Case Studies

The case studies presented in this section are examples of basic ECoN21 usage and interpretation with no in-depth analysis made. The output listings produced by ECoN21 for these examples are available as Supplementary Materials.

4.1. Rathite (Phase 'rath7')—Example of Site Population 'Bracketing'

The crystal structure of phase 'rath7': $Ag_{1.89}Tl_{2.16}Pb_{7.79}(As_{19.08}Sb_{0.96})_{20.04}S_{40.11}$, $P2_1/c$, a 8.484, b 7.961 c 25.031Å, β 100.66° (Topa and Kolitsch [34]) contains two mixed positions with Pb and Tl, namely, Pb1–Tl1 and Pb2–Tl2 (M1 and M2 hereafter) (Figure 4).

Both positions are coordinated by nine sulfur atoms in the form of tricapped trigonal prisms. Since Pb and Tl are indistinguishable in X-ray diffraction, the authors made no attempts to establish the site populations for these sites during the structure refinement. Based on the comparison of bond distances around M1 and M2 in samples that were isostructural with 'rath7', but with lower Tl content, Topa and Kolitsch [34] established a positive correlation between the Tl concentration and the increase of bond distances for the two positions.The shortest bond distances in M1 and M2 were better separated in Tl-rich rathite structures than in the Tl-poor ones, with the minimum distance in M1 exceeding the one in M2 by 0.05Å. Based on these observations, the authors assumed that M1 incorporated more Tl than M2.

From a CD and BVS point of view, due to the heterovalent character of the Pb^{2+}–Tl^{1+} substitution, one might expect a better or worse response of the calculation to different partitions of Pb and Tl assigned to M1 and M2 positions. A set of 12 virtual mixtures of Pb and Tl in M1 and M2 were introduced in separate input CIF files and computed with ECoN21 (Supplementary Materials S1). The 'mix1' and 'mix12' represent the extremes of the variable Pb–Tl proportions (i.e., the 'bracketing' limits). In 'mix1', the M1 position is occupied solely by Pb whereas M2 is occupied by the maximum amount of Tl per asymmetric unit (0.54), plus Pb to achieve complete occupancy. The rest of Pb goes to the split position As–Pb6. At the other end, Pb occupies the M2 position entirely while M1 is

set to contain the maximum available Tl and complementary Pb. The intermediate mixtures have decreasing contents of Pb in M1 and increasing Pb in M2, in steps of 0.05 atomic units.
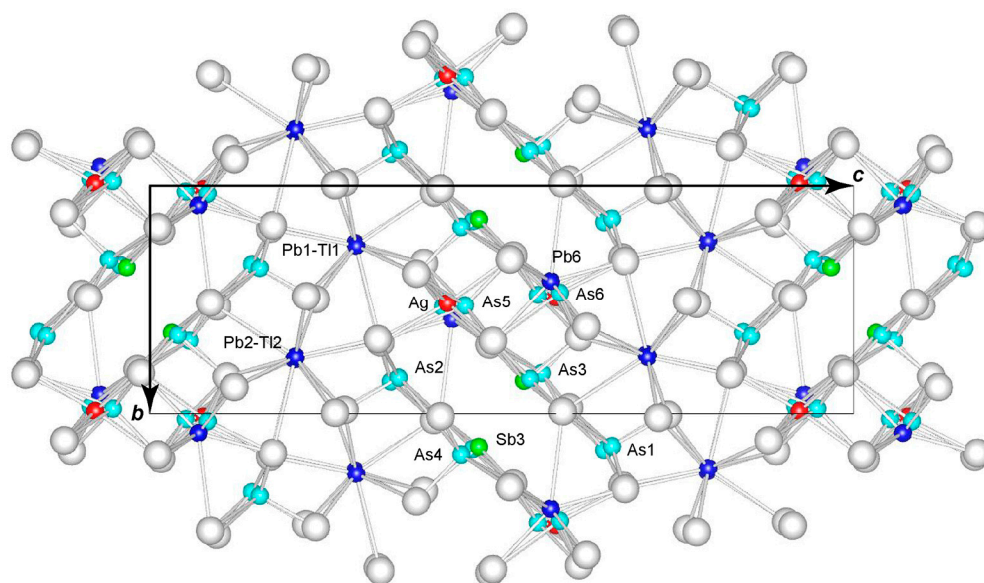

Figure 4. The crystal structure of phase 'rath7' (Topa and Kolitsch [34]) with labeled metal positions. White circles represent sulfur atoms.

The calculation for all these mixtures was made in the cation-centered description and concerned both the global and local $MAPD$s for the computed charges of M1 and M2 ligands which are supposed to react to charge variations in the metal positions (Table 1).

The first set of $MAPD$s, calculated only for the ligands of M1, shows a general decrease in the deviations from Tl-poor to Tl-rich mixtures, with a minimum corresponding to mixture 9. A second set concerning the sulfur atoms of the M2 has similar behavior, with better values towards the Tl-rich mixtures. The combined effect of the two trends can be seen in the distribution of the $MAPD$s for the entire set of ligands (S1–S8) around M1 and M2, which shows a minimum corresponding to 'mix9': Pb1:0.6, Tl1:0.4 in M1, Pb2:0.86 and Tl2:0.14 in M2 (Figure 5a). A similar trend is shown by the global (S1–S10) $MAPD$ for Q_A.
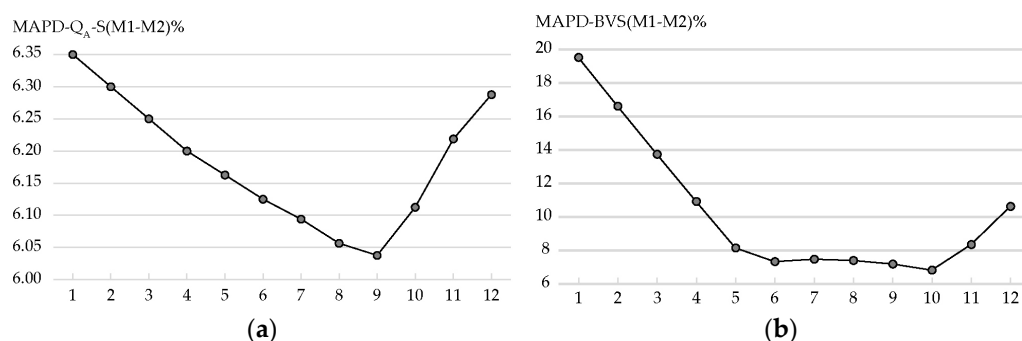

Figure 5. The variation of CD- and BVS-$MAPD$ (%) for various site populations in M1 and M2 sites in the crystal structure of 'rath7' (Topa and Kolitsch [34]): (**a**) Q_A for ligands of M1 and M2 (S1–S8) in the cation-centered description; (**b**) BVS for M1 and M2 combined (see text and Table 1 for details). The numbers from 1 to 12 represent mixtures with different Pb–Tl ratios (Table 1).

Table 1. Total Q_A charges received by the sulfur atoms and *MAPD*s for various virtual mixtures of Pb and Tl, in the Pb1–Tl1 (M1) and Pb2–Tl2 (M2) positions of the 'rath7' crystal structure (Topa and Kolitsch [34]). Lower *MAPD* values reflect a closer match between the formal and calculated charges.

		Mixtures											
		1	**2**	**3**	**4**	**5**	**6**	**7**	**8**	**9**	**10**	**11**	**12**
	Pb1	1.00	0.95	0.90	0.85	0.80	0.75	0.70	0.65	0.60	0.55	0.50	0.46
M1	Tl1	0.00	0.05	0.10	0.15	0.20	0.25	0.30	0.35	0.40	0.45	0.50	0.54
	charge	2.00	1.95	1.90	1.85	1.80	1.75	1.70	1.65	1.60	1.55	1.50	1.46
	Pb2	0.46	0.51	0.56	0.61	0.66	0.71	0.76	0.81	0.86	0.91	0.96	1.00
M2	Tl2	0.54	0.49	0.44	0.39	0.34	0.29	0.24	0.19	0.14	0.09	0.04	0.00
	charge	1.46	1.51	1.56	1.61	1.66	1.71	1.76	1.81	1.86	1.91	1.96	2.00
		Q_A											
	S1	−1.98	−1.98	−1.98	−1.98	−1.98	−1.98	−1.98	−1.98	−1.98	−1.98	−1.99	−1.99
	S2	−2.04	−2.04	−2.03	−2.03	−2.03	−2.03	−2.02	−2.02	−2.02	−2.02	−2.01	−2.01
	S3	−2.08	−2.07	−2.06	−2.05	−2.04	−2.03	−2.02	−2.01	−2.00	−1.99	−1.98	−1.97
	S4	−2.01	−2.02	−2.03	−2.04	−2.05	−2.06	−2.07	−2.08	−2.09	−2.10	−2.11	−2.12
	S5	−2.33	−2.33	−2.34	−2.34	−2.34	−2.34	−2.34	−2.35	−2.35	−2.35	−2.35	−2.35
	S6	−1.99	−2.00	−2.00	−2.00	−2.00	−2.00	−2.00	−2.01	−2.01	−2.01	−2.01	−2.01
	S7	−2.14	−2.14	−2.14	−2.13	−2.13	−2.12	−2.12	−2.11	−2.11	−2.10	−2.10	−2.10
	S8	−1.61	−1.61	−1.61	−1.62	−1.62	−1.62	−1.62	−1.62	−1.63	−1.63	−1.63	−1.63
		CD-*MAPD* (%)											
	Q_AS (M1) [1]	5.15	5.01	4.87	4.73	4.60	4.49	4.38	4.26	4.15	4.20	4.26	4.30
	Q_AS (M2) [2]	6.61	6.66	6.71	6.76	6.83	6.91	6.98	7.06	7.14	7.22	7.30	7.36
	Q_AS (M1–M2) [3]	6.35	6.30	6.25	6.20	6.16	6.13	6.09	6.06	6.04	6.11	6.22	6.29
CC [4]	Q_X	2.94	2.96	2.99	3.01	3.04	3.06	3.08	3.10	3.12	3.14	3.16	3.18
	Q_A	6.67	6.63	6.59	6.55	6.51	6.49	6.46	6.44	6.41	6.49	6.56	6.62
		BVS−*MAPD* (%)											
	M1	23.85	21.90	19.79	17.57	15.22	12.74	10.18	7.39	4.44	1.29	2.07	4.86
	M2	15.21	11.32	7.69	4.29	1.08	1.93	4.77	7.40	9.95	12.36	14.64	16.40
	M1–M2	19.53	16.61	13.74	10.93	8.15	7.34	7.47	7.40	7.19	6.82	8.35	10.63

[1] *MAPD*s for ligands of M1; [2] *MAPD*s for ligands of M2; [3] *MAPD*s for ligands of M1 and M2 positions combined; [4] Global *MAPD*s in the cation-centered description.

The same type of calculation was carried out for BVS. Various proportions of Tl and Pb in M1 and M2 produced different BVS values, more or less close to the formal oxidation numbers. For M1, the lowest *MAPD* for BVS occurs at 'mix10' (Pb1:0.55, Tl1:0.45, Pb2:0.91, Tl2:0.09), whereas for M2, at 'mix5' (Pb1:0.75, Tl1:0.25, Pb2:0.71, Tl2:0.29). The combined *MAPD* for BVS from the two positions taken together shows an interval of low values between 'mix6' and 'mix10' (Figure 5b).

By carrying out CD and BVS calculations with multiple inputs and by comparing the resulting *MAPD*s, the most likely compositional configurations of the M1 and M2 sites could be identified. In general, these configurations of 'optimal' mixtures sustain the idea of Topa and Kolitsch on a higher Tl content in M1.

4.2. Mutnovskite—From Homoligand and Heteroligand Perspective

Heteroligand structures in the cation-centered description are rare in the sulfosalt group. Selenium, oxygen, chlorine, iodine, and bromine are among the anions which may add to sulfur in the coordination polyhedra. Usually, the participation of such special anions is low and one might consider that by treating the structure as homoligand, the CD analysis would produce acceptable results. However, this is not always the case.

The crystal structure of mutnovskite (Zelenski et al. [35]): $Pb_2(As,Bi)(S,Se)_3(I,Cl,Br)$, *Pnma*, with *a* 11.543, *b* 6.6764, *c* 9.359 Å, contains two heteroligand tricapped trigonal prisms formed by (S,Se) and (I,Cl,Br) around two Pb positions (Figure 6). The trigonal prism of

Pb2 is incomplete ($CN = 8$) with the missing vertex occupied by an (As,Bi) position located at a rather unusually short distance from Pb2 (3.35 Å). The mixed halogen ligands of Pb1 form a trigonal planar HSP, whereas two such ligands form a dumbbell HSP around Pb2 (Figure 6). The (As,Bi) atom is coordinated by three (S,Se) ligands and occupies the apex of a trigonal pyramid. The coordination radius limits were set to 4.0 Å for Pb and to 3.0 Å for As–Bi. If the coordination polyhedra of Pb1 and Pb2 are treated as homoligand then the calculation of CD yields unacceptable results for Q_A (Table 2).

Table 2. Bond distances (R_{ij}), bond weights (w_{ij}), $ECoN_X$, calculated charges (Q_X, Q_A), and *MAPD* (%) for mutnovskite (Zelenski et al. [35]) in cation-centered, homoligand, and heteroligand approaches.

Cations	CN	Ligands	R_{ij}	Homoligand				Heteroligand			
				w_{ij}	Anions	Q_A	Q_X	w_{ij}	Anions	Q_A	Q_X
Pb1	9	S–Se2	2.760	1.403	S–Se1	–2.147	2.024	1.252	S–Se1	–2.108	2.021
		S–Se1	2.853	1.211	S–Se2	–2.016		1.054	S–Se2	–1.889	
		S–Se1	2.853	1.211	I–Cl–Br	–0.691		1.054	I–Cl–Br	–1.001	
		S–Se2	3.194	0.553				0.421			
		S–Se1	3.637	0.085				0.047			
		S–Se1	3.637	0.085				0.047			
		I–Cl–Br	3.534	0.323				1.220			
		I–Cl–Br	3.570	0.122				0.846			
		I–Cl–Br	3.570	0.122				0.846			
			$ECoN_1$:	5.115				$ECoN_1$:	6.785		
Pb2	8	S–Se1	2.907	1.402			2.121	1.371			1.968
		S–Se1	2.907	1.402				1.371			
		S–Se1	3.269	0.712				0.680			
		S–Se1	3.269	0.712				0.680			
		S–Se2	3.447	0.431				0.405			
		S–Se2	3.447	0.431				0.405			
		I–Cl–Br	3.047	1.128				1.226			
		I–Cl–Br	3.446	0.432				0.515			
			$ECoN_2$:	6.648				$ECoN_2$:	6.652		
As–Bi	3	S–Se1	2.241	1.004			2.855	1.004			3.011
		S–Se1	2.241	1.004				1.004			
		S–Se2	2.246	0.992				0.992			
			$ECoN_3$:	3.000				$ECoN_3$:	3.000		
MAPD						13.01	4.03			3.69	1.02

In the homoligand approach, for each Pb polyhedron, the bond weights are ranked based on the shortest distance alone (2.760 and 2.907 Å, respectively). The Pb–halogen distances are comparatively longer and so, they rank among the weakest bonds in the polyhedron and will result in a severely underestimated charge for (I,Cl,Br): −0.691 vs. −1.0. The deficit of charge for the halogen position will reflect in the overbonding of cations in neighboring polyhedra, and the excessive Q_X of Pb2 (2.121 vs. 2.0) is most likely a sign of that.

If the CD analysis is carried out in the heteroligand approach, the bond weights are ranked separately for (S,Se) and (I,Cl,Br), the latter being assigned considerably higher bond weights. The $ECoN_X$ of Pb1 is increased from 5.115 to 6.785, whereas for Pb2 there is only a slight increase in this value. In the case of Pb2, a much shorter distance of 3.047 Å to (I,Cl,Br) with a bond weight of 1.128 in the homoligand ranking contributes to a higher $ECoN_X$ and a smaller difference from the heteroligand $ECoN_X$. The results obtained for the heteroligand description are better and fully acceptable (Supplementary Materials S2).
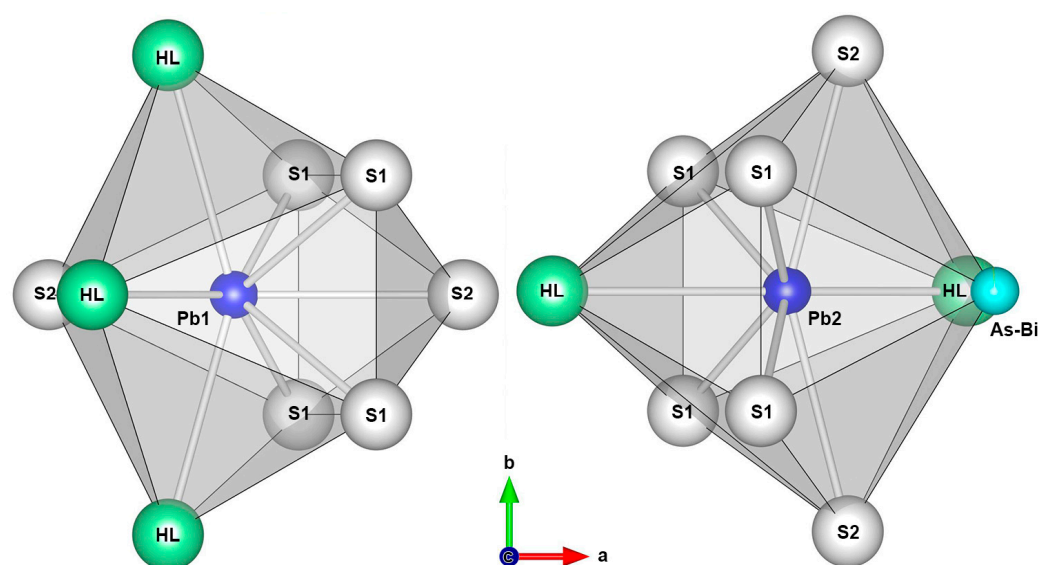
Figure 6. The heteroligand tricapped trigonal prisms around Pb1 and Pb2 in the crystal structure of mutnovskite (Zelenski et al. [35]). HL denotes the mixed halogen ligands with I–Cl–Br and S1, S2 represent mixed (S,Se). The As–Bi position is located in a 'vacant' vertex of the Pb2 tricapped prism.

4.3. Dalnegroite—The Propagation of Local CD Anomalies

Dalnegroite—$Tl_{5-x}Pb_{2x}(As,Sb)_{21-x}S_{34}$ (Bindi et al. [18]) has a homoligand cation-centered crystal structure for which the CD calculation should be straightforward. However, in this description, the *MAPD*s are very high: 12.74% (Q_X) and 24.03% (Q_A) (Supplementary Materials S3). The CD analysis reveals several underbonded cations of which two stand out: Sb22 (Q_X 1.48 vs. q_X 3.00) and Sb24 (Q_X 1.42 vs. q_X 3.00). Such severely underbonded central atoms suggest extreme internal distortions in host polyhedra and the existence of few effective bonds. Indeed, in each Sb22 and Sb24 polyhedra, there is only one functional bond, all the others delivering close to zero bond weights (Figure 7).

Therefore, the charge of Sb22 and Sb24 is distributed only to S72 and S78, respectively, regardless of the chosen coordination threshold. The first effect is that these ligands receive Q_A charges exceeding over twice their formal oxidation numbers. In opposition, the Q_A charges for weakly or non-bonded ligands such as S70, S76, S126, and S13 will yield lower than normal values. However, the inverse proportionality between Q_X and Q_A (Equation (7)) contributes to a higher positive charge of neighboring central atoms sharing weakly bonded ligands with Sb22 and Sb44, especially if such satellite central atoms have short bonds to these ligands, i.e., with high $\Delta q_{Xij \to A}$. Some of the most severely overbonded central positions in dalnegroite have ligands bearing zero-weight bonds to Sb22 and Sb24, e.g., Sb17 (Q_X 4.42 vs. q_X 3.00), Sb19 (4.56 vs. 3.00) Sb21 (4.38 vs. 3.00), etc.

In contrast to the underbonding pointed out by the CD, the BVS_X values associated with Sb22 and Sb24 are both very elevated (5.49 and 5.96 vs. 3.00). The reason behind this apparent contradiction is that the shortest bonds in both polyhedra are assigned abnormally high amounts of valence units (4.06 and 4.24) that account for 71% to 74% of the total BVS_X and which already exceed the formal oxidation numbers. In summary, the shortest distances in Sb22 and Sb24 CP appear to be simply too short.
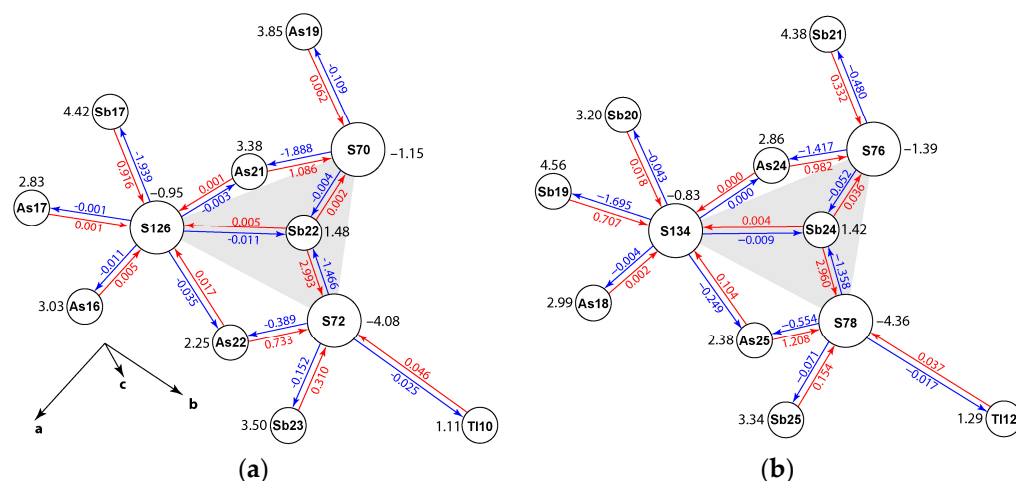
Figure 7. The charge distribution around Sb22 (**a**) and Sb24 (**b**) in the structure of dalnegroite (Bindi et al. [18]). Red values represent fractions of central atom charge distributed to the ligands ($\Delta q_{Xij \to A}$); the blue values are the partial charges received by the central atoms (ΔQ_{ij}). Shaded areas represent projections of the coordination trigonal pyramids built on the shortest distances of Sb22 and Sb24. An increase of the coordination radius threshold would have resulted in adding only zero−weight bonds to these polyhedra. The numbers near the atoms are the computed charges Q_X and Q_A to be compared with the formal oxidation numbers: +3 for As,Sb, +1 for Tl, and −2 for S.

Such extreme distortions do not occur in the anion-centered description and the results of the CD calculation are significantly better: 6.73% for Q_A and 10.57% for Q_X. However, the *MAPD* for cations remains high and requires attention. The observations on Sb22 and Sb24 are just examples of what can be inferred from the CD and BVS analysis. A complete examination should be extended to all the positions with deviating CD or BVS values.

4.4. ECoN and the Polyhedral Distortion

The very existence of an $ECoN_X$ smaller than CN_X denotes a certain degree of polyhedral distortion. A possible measure of this distortion—which exploits the actual results of the CD calculation—is the *deviation $EDEV_X$ of $ECoN_X$ from CNR_X* (Equation (24)) which reflects the scatter and range of distances between the central atom and its ligands (internal distortion) rather than the irregularity of the ligand distribution with respect to the best approximant sphere (external distortion). Hence, there should be a direct correlation between $EDEV_X$ and those geometric quantities which express the bond length variability. Several examples of As–, Sb– or Bi–sulfosalts with a large number of CP were used for comparing $EDEV_X$ to such quantities: incomsartorite—$Tl_6Pb_{144}As_{246}S_{516}$, $P2_1/n$, *a* 45.9944, *b* 7.8793, *c* 58.6716 Å, *β* 90.153° (Topa et al. [17]), argentoliveingite—$Ag_{3+x}Pb_{36-2x}As_{51+x}S_{112}$ (0 ≤ x < 0.5), $P\bar{1}$, a 7.905, b 8.469, c 137.96 Å, α 89.592, β 88.969, γ 89.893° (Topa et al. [16]), andorite VI—$PbAgSb_3S$, $Pna2_1$, *a* 12.949, *b* 25.550, *c* 19.225 Å (Topa, personal communication), Pb–chabournéite—$Ag_{0.04}Tl_{2.15}Pb_{0.64}Sb_{5.12}As_{5.05}S_{17.32}$, $P\bar{1}$, *a* 8.5197, *b* 42.461, *c* 16.293 Å, α 83.351, β 90.958, γ 84.275° (Biagioni et al. [7]), synthetic cannizzarite—$Pb_{46}Bi_{54}S_{127}$, $P2_1/m$, *a* 189.8, *b* 4.09, *c* 74.06 Å, *β* 11.93° (Matzat [36]), Sb–rich gustavite—$AgPb(Bi_2Sb)_3S_6$, $P2_1/c$, *a* 7.0455, *b* 19.5294, *c* 8.3412 Å, *β* 107.446° (Pažout and Dušek [37]), isotypic with later accredited terrywallaceite, but with different Sb–Bi site populations, terrywallaceite—$AgPb(Sb,Bi)_3S_6$, $P2_1/c$, *a* 6.9764, *b* 19.351, *c* 8.3870 Å, *β* 107.519° (Yang et al. [38]), and Sb–rich vikingite—$Ag_{2.85}Pb_{12.35}(Bi_{9.52}Sb_{1.27})_{\sum=10.80}S_{30}$, $C2/m$, *a* 13.5394, *b* 4.0992, *c* 25.506 Å, *β* 95.597° (Pažout and Dušek [39]). Calculation data for these phases are given in Supplementary Materials S4 to S11.

Incomsartorite is an 11-fold approximant superstructure of the subcell of N = 3 sartorite homologues. It contains 33 tricapped trigonal coordination prisms fully occupied by Pb(Tl), 19 mixed Pb–As positions, and 47 As atoms (Topa, personal communication) with CD-based coordination numbers from 3 to 5. Positive correlations are obvious between $EDEV_X$ and the standard deviation of distances from the central atom to the ligands, the

displacement of the central atom from the centroid, the 'volume-based' eccentricity of the LSF sphere, and the Baur and Brown distortion indexes. Two examples are shown in Figure 8. No correlation exists between $EDEV_X$ and external deformation parameters such as the standard deviation of distances from the centroid to ligands, the sphericity, or the polyhedral volume distortion (v). The correlations with internal distortion parameters differ with the type of central atom.
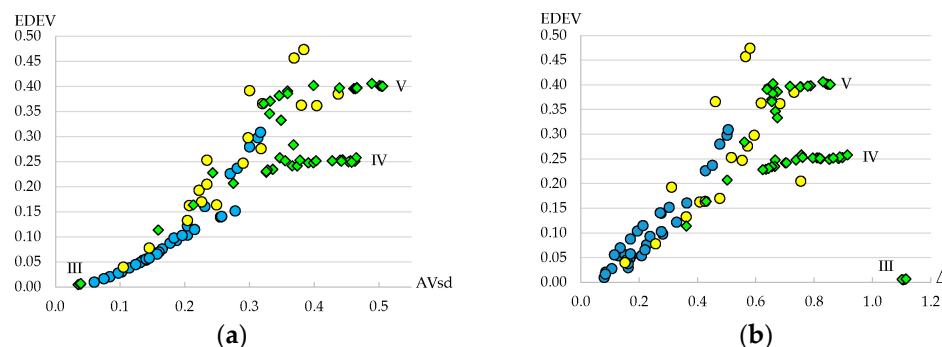

Figure 8. Correlations between $EDEV_X$ and internal distortion parameters of incomsartorite (Topa et al. [17]; structure data by courtesy of Dan Topa): (**a**) standard deviation of distances—$AVsd$, (**b**) displacement of the central atom from the centroid—Δ. Blue circles represent Pb, yellow circles are mixed As–Pb positions, and green diamonds are pure As sites. Roman numerals denote coordination numbers of As.

For Pb and mixed As–Pb, these correlations are approximately linear and well expressed. Instead, for pure As positions, $EDEV_X$ modifies only slightly for a given coordination number (i.e., 3, 4, or 5: average $EDEV_X$: 0.006, 0.236, and 0.381, respectively). Similar behavior of As polyhedra is found in other As-bearing sulfosalts: e.g., argentoliveingite (average $EDEV_X$: 0.010, 0.257, 0.311), Pb-rich chabournéite (average $EDEV_X$: 0.009, 0.254, 0.397), etc. (Figure 9). This peculiar feature of As is caused by its three persistently short distances which account for over 99% of the $ECoN_X$. While the rest of the weaker bonds—with w_{ij} above 0.001—add to CNR_X, they do not add significantly to $ECoN_X$ and hence $EDEV_X$ tends to be quasi-constant for a given CNR_X.
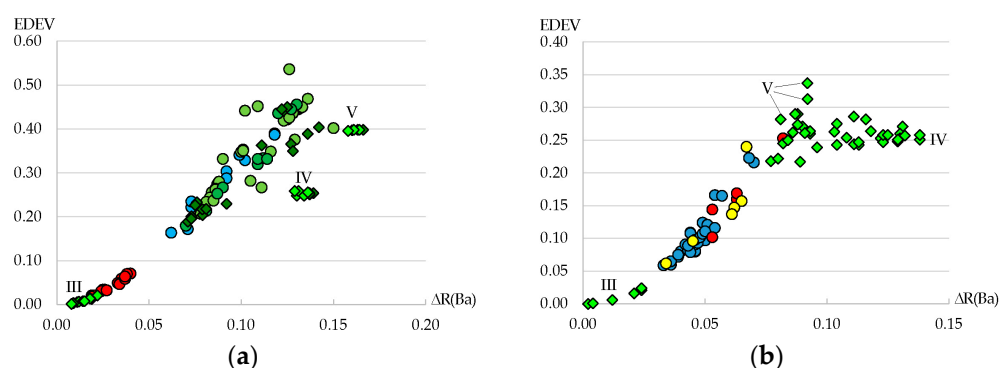
Figure 9. Correlations between $EDEV_X$ and Baur distortion index—$\Delta R(Ba)$ for (**a**) Pb–chabournéite (Biagioni et al. [7]) and (**b**) argentoliveingite (Topa et al. [16]). Blue circles denote Pb, red circles represent Tl (**a**) or Ag (**b**); light−green circles in (**a**) are Sb positions, dark−green diamonds are mixed As–Sb positions, yellow circles are mixed Pb–As sites and light green diamonds are pure As positions. Roman numerals denote the coordination of As.

Andorite VI ('senandorite') was chosen to illustrate $EDEV_X$ correlations in Sb–sulfosalts. Its crystal structure (Topa, personal communication) belongs to the lillianite homologous series and represents a six-fold superstructure of the 4 Å andorite subcell described by Kawada and Hellner [40]. Antimony forms coordination octahedra with three short and

three long distances and with centroids placed in the lone electron pair volume of the polyhedra, at distances between 0.193–0.903 Å from the central atoms. The correlation of $EDEV_X$ with the 'volume-based' eccentricity is shown in Figure 10a. The proportionality between $EDEV_X$ and other internal distortion parameters of Sb polyhedra is much more obvious than in the case of As. Due to a decreasing growth rate of $EDEV_X$ with increasing ´volume-based´ eccentricity, the reciprocity in Figure 10a is not entirely linear. Such correlations show that $EDEV_X$ may be efficiently employed for assessing the internal deformation of CP even if used as an independent parameter (Figure 10b).
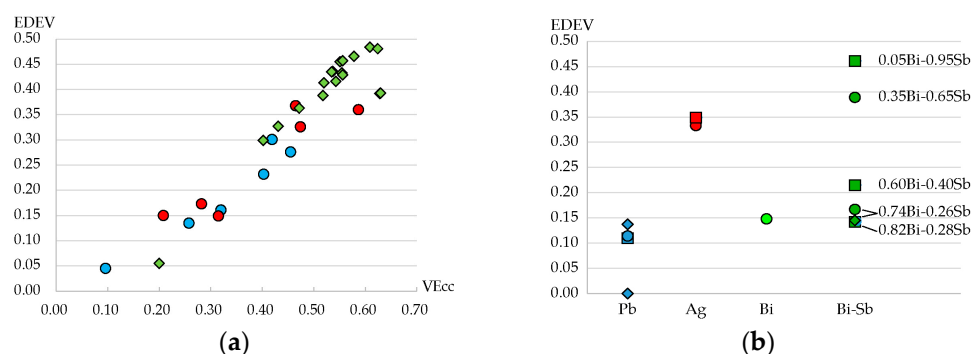
Figure 10. (**a**): Correlation between $EDEV_X$ and 'volume-based' eccentricity—$VEcc$ in andorite VI ('senandorite') (Topa, personal communication); (**b**) $EDEV_X$ values for Pb, Ag, Bi, and Bi–Sb polyhedra in Sb–rich gustavite (Pažout and Dušek [37]) (circles), terrywallaceite (Yang et al. [38]) (squares), and Sb–rich vikingite (Pažout and Dušek [39]) (diamonds). The polyhedra with mixed central positions, display progressively higher $EDEV_X$ with higher Sb content. Blue points represent Pb, red points—Ag, light−green points—Bi or Sb, and dark−green points—mixed Bi-Sb.

Bi–sulfosalts have lower distortions in semimetal polyhedra and therefore, the reciprocity between $EDEV_X$ and other quantities expressing the internal distortion develop at much lower values (Figure 11). Synthetic cannizzarite (Matzat [36]) shows a narrow range of $EDEV_X$ which barely reaches values of 0.3. The two branches visible in the distribution of Bi in Figure 11a correspond to the H (PbS) and Q (SnS) layers in the crystal structure. A separation also exists between the Pb polyhedra: the ones in the Q layers (mostly mono-or bicapped trigonal prisms) show higher distortion than those in the H layers (octahedra), with the latter narrowly exceeding values of 0.05 $EDEV_X$.
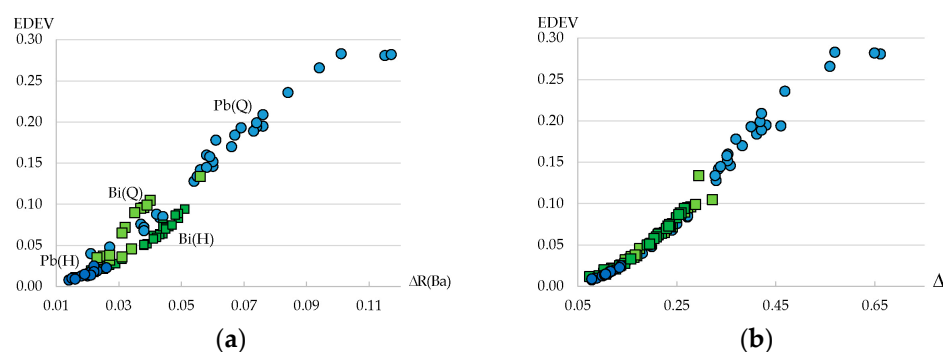
Figure 11. Correlations between $EDEV_X$ and (**a**) the Baur distortion index—$\Delta R(Ba)$, and (**b**) the displacement of the centroid—Δ, for synthetic cannizzarite (Matzat [36]). Blue points denote Pb and the green ones, Bi. Darker hues correspond to atom positions in the H layers of the crystal structure.

A synoptic view of $EDEV_X$ ranges and average values for a selection of CP in over 170 sulfosalt crystal structures is shown in Figure 12. The list of crystal structures used for this figure is included in Supplementary Materials S12.
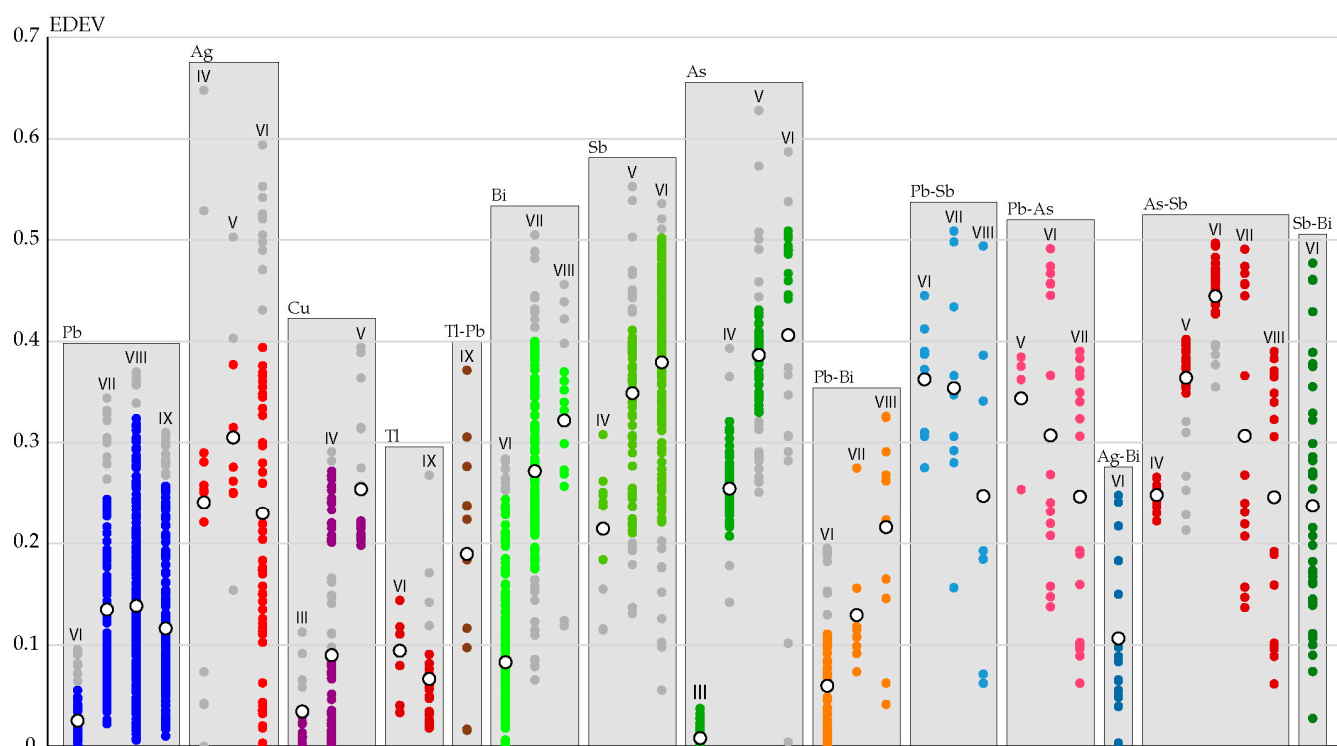
Figure 12. Ranges and average values of $EDEV_X$ for a selection of CP in over 170 sulfosalt crystal structures. Roman numerals denote the *CN* determined by non-zero bond weights of the central atoms indicated at the top of the grey rectangles. Binary mixed central positions for which sufficient data were available are also given. Colored clusters denote 'significant' groups accounting for at least 80% of the entire sets of values (applies to polyhedra with sufficient data). Grey circles are singular or less frequent values and describe the overall limits for each type of central atom and *CN*. White circles are average values.

As a tendency, except for Ag, metals such as Pb, Cu, and Tl have low $EDEV_X$ values, rarely and slightly over 0.3. Among semimetals, the six-fold coordinated Bi and the three-fold coordinated As polyhedra are the least distorted. The value of $EDEV_X$ for semimetals in octahedral coordination increase from Bi to Sb and As. For similar coordinations, As is more distorted than Sb. $EDEV_X$ also increases with the coordination number of the same semimetal species. Polyhedra of As show the same tight clustering around quasi-constant $EDEV_X$, with significant values spanning slightly over a range of 0.1. The average $EDEV_X$ for various *CN*s are: 0.009 (III), 0.255 (IV), 0.387 (V), and 0.406 (VI). Mixed Pb–Sb and Pb–As display lower $EDEV_X$ values for higher *CN*s. Since both As and Sb tend to form CP with low *CN*, it is reasonable to assume that higher *CN*s are dominated by Pb which natively forms less distorted polyhedra.

5. Conclusions

The CD and BVS methods are appropriate and sensitive aids in analyzing the quality of the crystal structure determination and in interpreting the isomorphism of mixed positions. In the majority, mineral sulfosalts are characterized by a substantial presence of distorted CP which makes this group of minerals suitable for the CD and BVS methods.

Contrary to the BVS method, which uses empirical exponential curves uniquely defined for specific pairs of cations and anions, to describe the variation of bond strengths vs. bond lengths, the CD method involves exponential decrease laws which depend on the distribution of bond lengths in each CP. The ECoN21 program presented in this paper wraps calculations for the two methods as well as for an extensive set of geometric and distortion parameters of the CP, most of which are derived from the concept of the centroid (Makovicky and Balić–Žunić [28,29]).

Since there is no unique way to define the coordination radius, the program gives a wide choice of options to adjust this parameter: (a) global coordination radius threshold; (b) chemical bond-specific thresholds; (c) custom, polyhedron-specific thresholds. The coordination radius can be automatically limited by the distance to the nearest central atom or can be set to include only non-zero bond weights.

The interpretation of the CD and BVS results is made in very simple terms: i.e., how much the computed charges of the central atoms (Q_X) and their ligands (Q_A) deviate from the formal oxidation numbers—q_X and q_A—of these atoms. Such deviations—measured for the central atoms—may point out problematic features of the crystal structure determination, whereas the departure of ligand computed charges from their formal oxidation number reflect the induced over- or underbonding effects (Nespolo et al. [11,12]). A similar match should be obtained between the BVS_X and the formal oxidation number of the central atom. The CD and valence state of local or global clusters of polyhedra may be evaluated using the $MAPD$ for the computed charges (Q_X, Q_A) and BVS_X.

The deviation of $ECoN_X$ from the CD-based coordination number CNR_X may be used as an independent measure of the internal polyhedral distortion and, to a certain extent, for distinguishing among various chemical types of atoms in the structure.

The CD and BVS methods described in the paper bring out global and local features of the crystal structure which would otherwise be difficult to observe. The ECoN21 program greatly simplifies the approach to these two methods.

References

1. Brown, I.D. Bond valences—A simple structural model for inorganic chemistry. *Chem. Soc. Rev.* **1978**, *7*, 359–376. [CrossRef]
2. Brown, I.D. *The Chemical Bond in Inorganic Chemistry. The Bond Valence Model*; Cambridge University Press: Cambridge, UK, 2002; pp. 1–278.

3.   Brown, I.D. Recent developments in methods and applications of the bond valence model. *Chem. Rev.* **2009**, *109*, 6858–6919. [CrossRef] [PubMed]

4.   Orlandi, P.; Biagioni, C.; Moëlo, Y.; Bonaccorsi, E.; Paar, W.H. Lead–Antimony sulfosalts from Tuscany (Italy). XIII. Protochabournéite, ~$Tl_2Pb(Sb_{9-8}As_{1-2})_{\Sigma 10}S_{17}$, from the Monte Arsiccio mine: Occurrence, crystal structure, and relationship with chabournéite. *Can. Mineral.* **2013**, *51*, 475–494. [CrossRef]

5.   Biagioni, C.; Bonaccorsi, E.; Moëlo, Y.; Orlandi, P.; Bindi, L.; D'Orazio, M.; Vezzoni, S. Mercury–arsenic sulfosalts from the Apuan Alps (Tuscany, Italy). II. Arsiccioite, $AgHg_2TlAs_2S_6$, a new mineral from the Monte Arsiccio mine: Occurrence, crystal structure and crystal chemistry of the routhierite isotypic series. *Mineral. Mag.* **2014**, *78*, 101–117. [CrossRef]

6.   Biagioni, C.; Orlandi, P.; Moëlo, Y.; Bindi, L. Lead–antimony sulfosalts from Tuscany (Italy). XVI. Carducciite, $(Ag,Sb)Pb_6(As,Sb)_8S_{20}$, a new Sb–rich derivative of rathite from the Pollone mine, Valdicastello Carducci: Occurrence and crystal structure. *Mineral. Mag.* **2014**, *78*, 1775–1793. [CrossRef]

7.   Biagioni, C.; Moëlo, Y.; Favreau, G.; Bourgoin, V.; Boulliard, J.-C. Structure of Pb–chabournéite from Jas Roux, France. *Acta Crystallogr.* **2015**, *71*, 81–88. [CrossRef]

8.   Brese, N.E.; O'Keeffe, M. Bond–Valence Parameters for Solids. *Acta Crystallogr.* **1991**, *47*, 192–197. [CrossRef]

9.   Hoppe, R. Effective coordination numbers (ECoN) and mean fictive ionic radii (MEFIR). *Z. Kristallogr.* **1979**, *150*, 23–52. [CrossRef]

10. Hoppe, R.; Voigt, S.; Glaum, H.; Kissel, J.; Müller, H.P.; Bernet, K. A new route to charge distributions in ionic solids. *J. Less–Comm. Met.* **1989**, *156*, 105–122. [CrossRef]

11. Nespolo, M.; Ferraris, G.; Ohashi, H. Charge distribution as a tool to investigate structural details: Meaning and application to pyroxenes. *Acta Crystallogr.* **1999**, *55*, 902–916. [CrossRef]

12. Nespolo, M.; Ferraris, G.; Ivaldi, G.; Hoppe, R. Charge distribution as a tool to investigate structural details. II. Extension to hydrogen bonds, distorted and hetero–ligand polyhedra. *Acta Crystallogr.* **2001**, *57*, 652–664. [CrossRef] [PubMed]

13. Eon, J.-G.; Nespolo, M. Charge distribution as a tool to investigate structural details. III. Extension to description in terms of anion–centered polyhedral. *Acta Crystallogr.* **2015**, *71*, 34–47.

14. Nespolo, M.; Guillot, B. CHARDI2015: Charge distribution analysis of non-molecular structures. *J. Appl. Crystallogr.* **2016**, *49*, 317–321. [CrossRef]

15. Nespolo, M. Charge distribution as a tool to investigate structural details. IV. A new route to heteroligand polyhedra. *Acta Crystallogr.* **2016**, *72*, 51–66. [CrossRef] [PubMed]

16. Topa, D.; Kolitsch, U.; Graeser, S.; Makovicky, E.; Stanley, C.J. Argentoliveingite, $Ag_{3+x}Pb_{36-2x}As_{51+x}S_{112}$ ($0 \leq x <0.5$), a new homeotype of liveingite from Lengenbach, Binntal, Switzerland, and the crystal chemistry of the liveingite group. *Eur. J. Mineral.* **2019**, *31*, 1079–1097.

17. Topa, D.; Stoeger, B.; Makovicky, E.; Stanley, C. Incomsartorite, IMA 2016–035. CNMNC Newsletter No.33, October 2016. *Mineral. Mag.* **2016**, *80*, 1135–1144.

18. Bindi, L.; Nestola, F.; Guastoni, A.; Secco, L. The crystal structure of dalnegroite, $Tl_{5-x}Pb_{2x}(As,Sb)_{21-x}S_{34}$: A masterpiece of structural complexity. *Mineral. Mag.* **2010**, *74*, 999–1012. [CrossRef]

19. Momma, K.; Izumi, F. VESTA 3 for three–dimensional visualization of crystal, volumetric, and morphology data. *J. Appl. Crystallogr.* **2011**, *44*, 1272–1276. [CrossRef]

20. Pauling, L. The principles determining the structure of complex ionic crystals. *J. Am. Chem. Soc.* **1929**, *51*, 1010–1026. [CrossRef]

21. Topa, D.; Makovicky, E.; Dittrich, H. The crystal structure of 7H:12Q cannizzarite from Vulcano, Italy. *Can. Mineral.* **2010**, *48*, 483–495. [CrossRef]

22. Ferraris, G. Inorganic and mineral crystals. In *Fundamentals of Crystallography*, 3rd ed.; Giacovazzo, C., Ed.; Oxford University Press: Oxford, UK, 2011; pp. 512–591.

23. Brown, I.D.; Altermatt, D. Bond–Valence Parameters Obtained from a Systematic Analysis of the Inorganic Crystal Structure Database. *Acta Crystallogr.* **1985**, *41*, 244–247. [CrossRef]

24. Brown, I.D. Accumulated List of Bond Valence Parameters. 2020. Available online: https://www.iucr.org/resources/data/datasets/bond-valence-parameters (accessed on 15 July 2022).

25. Gagné, O.C.; Hawthorne, F.K. Comprehensive derivation of bond-valence parameters for ion pairs involving oxygen. *Acta Crystallogr.* **2015**, *71*, 562–578.

26. Bosi, F. Bond valence at mixed occupancy sites. I. Regular polyhedra. *Acta Crystallogr.* **2014**, *70*, 864–870. [CrossRef]

27. Brown, I.D. On measuring the size of distortions in coordination polyhedra. *Acta Crystallogr.* **2006**, *62*, 692–694. [CrossRef] [PubMed]

28. Makovicky, E.; Balić–Žunić, T. New Measure of Distortion for Coordination Polyhedra. *Acta Crystallogr.* **1998**, *54*, 766–773. [CrossRef]

29. Makovicky, E.; Balić–Žunić, T. Determination of the Centroid or 'the Best Centre' of a Coordination Polyhedron. *Acta Crystallogr.* **1996**, *52*, 78–81.

30. Balić–Žunić, T.; Vicković, I. IVTON–Program for the calculation of geometrical aspects of crystal structures and some crystal–chemical applications. *J. App. Crystallogr.* **1996**, *29*, 305–306. [CrossRef]

31. Topa, D.; Makovicky, E.; Balić–Žunić, T. Crystal structures and crystal chemistry of members of the cuprobismutite homologous series of sulfosalts. *Can. Mineral.* **2003**, *41*, 1481–1501. [CrossRef]

32. Baur, W.H. The Geometry of Polyhedral Distortions. Predictive Relationships for the Phosphate Group. *Acta Crystallogr.* **1974**, *30*, 1195–1215.

33. Petříček, V.; Dušek, M.; Palatinus, L. Crystallographic Computing System JANA2006: General features. *Z. Kristallogr.* **2006**, *229*, 345–352. [CrossRef]

34. Topa, D.; Kolitsch, U. The Crystal Chemistry of Rathite Based on New Electron–Microprobe Data and Single–Crystal Structure Refinements: The Role of Thallium. *Minerals* **2018**, *8*, 466. [CrossRef]

35. Zelenski, M.; Balić–Žunić, T.; Bindi, L.; Garavelli, A.; Makovicky, E.; Pinto, D.; Vurro, F. First occurrence of iodine in natural sulfosalts: The case of mutnovskite, $Pb_2AsS_3(I,Cl,Br)$, a new mineral from the Mutnovsky volcano, Kamchatka Peninsula, Russian Federation. *Am. Mineral.* **2006**, *91*, 21–28. [CrossRef]

36. Matzat, E. Cannizzarite. *Acta Crystallogr.* **1979**, *35*, 133–136. [CrossRef]

37. Pažout, R.; Dušek, M. Natural monoclinic $AgPb(Bi_2Sb)_3S_6$, an Sb–rich gustavite. *Acta. Crystallogr.* **2009**, *65*, i77–i80. [CrossRef] [PubMed]

38. Yang, H.; Downs, R.T.; Evans, S.H.; Pinch, W.W. Terrywallaceite, $AgPb(Sb,Bi)_3S_6$, isotypic with gustavite, a new mineral from in a Herminia, Julcani Mining District, Huancavelica, Peru. *Am. Mineral.* **2013**, *98*, 1310–1314. [CrossRef]

39. Pažout, R.; Dušek, M. Crystal structure of undersubstituted Sb–rich vikingite Vik_{40}, $Ag_{2.85}Pb_{12.35}(Bi_{9.52}Sb_{1.27})_{\sum=10.80}S_{30}$: Site population and comparison with the structure of vikingite Vik_{50}, $Ag_{3.5}Pb_{11.0}Bi_{11.5}S_{30}$. *J. Geosci.* **2021**, *66*, 175–184. [CrossRef]

40. Kawada, I.; Hellner, E. Die Kristallstruktur der Pseudozelle (subcell) von Andorit VI (Ramdohrit). *Neues Jahrb. Mineral. Mon.* **1971**, *1971*, 551–560.

41. Topa, D.; Makovicky, E. Argentobaumhauerite: Name, chemistry, crystal structure, comparison with baumhauerite, and position in the Lengenbach mineralization sequence. *Mineral. Mag.* **2016**, *80*, 819–840. [CrossRef]

42. Makovicky, E.; Topa, D.; Paar, W.H. The definition and crystal structure of clino-oscarkempffite, $Ag_{15}Pb_6Sb_{21}Bi_{18}S_{72}$. *Eur. J. Mineral.* **2008**, *30*, 569–589. [CrossRef]

43. Makovicky, E.; Topa, D.; Stoeger, B. The crystal structures of heptasartorite, $Tl_7Pb_{22}As_{55}S_{108}$, and enneasartorite, $Tl_6Pb_{32}As_{70}S_{140}$, two members of an anion–omission series of complex sulfosalts from Lengenbach, the Swiss Alps, and comparison with the structures of As–Sb sartorite homologues. *Eur. J. Mineral.* **2018**, *30*, 149–164. [CrossRef]

44. Makovicky, E.; Topa, D.; Stoeger, B.; Stanley, C.J. Heptasartorite, $Tl_7Pb_{22}As_{55}S_{108}$, enneasartorite, $Tl_6Pb_{32}As_{70}S_{140}$ and hendekasartorite, $Tl_2Pb_{48}As_{82}S_{172}$, three members of the anion–omission series of 'sartorites' from the Lengenbach quarry at Binntal, Wallis, Switzerland. *Eur. J. Mineral.* **2019**, *29*, 701–712.

45. Bindi, L.; Biagioni, C.; Neutsch, F.N. Oyonite, $Ag_3Mn_2Pb_4Sb_7As_4S_{24}$, a New Member of the Lillianite Homologous Series from the Uchucchacua Base–Metal Deposit, Oyon District, Peru. *Minerals* **2018**, *8*, 192. [CrossRef]